THE EDGE CRACKING AND SPALLING OF BRITTLE PLATES

M. D. THOULESS,[1] A. G. EVANS,[1] M. F. ASHBY[2] and J. W. HUTCHINSON[3]

[1]Materials Program, College of Engineering, University of California, Santa Barbara, CA 93106, U.S.A.
[2]University Engineering Department, Cambridge University, Cambridge CB2 1PZ, England and
[3]Division of Applied Sciences, Harvard University, Cambridge, MA 02139, U.S.A.

Abstract—The cracking and spalling processes that accompany the edge loading of brittle plates have been investigated. Experiments performed on glass and on PMMA have revealed systematic trends in crack location, crack propagation load, and in the onset of spalling. In particular, a steady state crack growth region has been identified wherein the cracks propagate parallel to the side surface. Calculations of mode I and mode II stress intensities have allowed comparison of the crack trajectories and crack propagation loads with experimental measurements. The general trends in cracking were found to be broadly consistent with predicted behavior governed by a zero mode II criterion and assuming that the cracks grow into a steady state trajectory. However, some quantitative discrepancies exist. These have been attributed to constraining tractions that develop upon distortion of the test specimens.

Résumé—Nous avons étudié les mécanismes de fissuration et d'écaillage qui accompagnent la mise en charge de plaques fragiles sur la tranche. Les expériences réalisées sur du verre et sur du PMMA ont révélé des tendances systématiques dans la localisation de la fissure, dans la charge de propagation de la fissure, et dans le début de l'écaillage. En particulier, nous avons identifié un domaine de croissance stationnaire de la fissure dans lequel les fissures se propagent parallèlement à la surface latérale. Le calcul des intensités de la contrainte dans les modes I et II ont permis de comparer les trajectoires des fissures et leurs charges de propagation avec les mesures expérimentales. La tendance générale à la fissuration est généralement compatible avec le comportement prédit en se basant sur l'hypothèse que les fissures grossissent en suivant une trajectoire stationnaire régie par un critère de zéro dans le mode II. Cependant, il y a quelques écarts quantitatifs que nous avons attribués à des tensions liées à la distorsion des éprouvettes d'essais.

Zusammenfassung—Die Bruch- und Abspaltprozesse, die bei der Kantenbelastung spröder Materialien auftreten, wurden untersucht. Die Experimente an Glas und PMMA weisen systematische Tendenzen in der Lage der Risse, der für Rißausbreitung notwendigen Last und dem Einsatz des Abspaltens auf. Insbesondere konnte ein Bereich des stationären Rißwachstums aufgefunden werden, in dem sich die Risse parallel zur Seitenfläche ausbreiten. Mit Berechnungen der Spannungsintensitäten für Mode I und Mode II konnten die Rißtrajektorien und die Lasten für Rißausbreitung mit den experimentellen Messungen verglichen werden. Die allgemeinen Tendenzen bei der Rißbildung stimmten gut mit dem vorausgesagten Verhalten überein, vorausgesetzt, daß die Risse in eine stationäre Trajektorie wachsen, bei der das Kriterium für Mode II zu Null wird.

1. INTRODUCTION

When a load is applied along the edge of a brittle plate, cracks may initiate, propagate and, eventually spall from the side surface (Fig. 1). Such edge dominated cracking and spalling phenomena have been encountered in many problems of technological importance: edge machining, edge mounting, the impact of ice sheets onto offshore structures [1], flint knapping [2], etc. Analogous edge cracking and decohesion processes have been noted in residually stressed thin films and coatings [3] used in various electronic devices, as well as in barrier coatings (Fig. 2). Yet apparently there has not been a systematic attempt to investigate either the nucleation and propagation of such cracks, or the ultimate spalling event. The present article addresses several of the issues central to these processes. Experiments performed on precracked plates, and related stress

intensity factor calculations contribute toward the understanding of crack propagation. In addition, stress analysis coupled with weakest link statistics provide a description of trends in crack nucleation. Finally, spalling is addressed by considering the critical event that deflects the crack to the surface.

2. EXPERIMENTS

2.1. Test procedures

Plate specimens of two transparent materials (PMMA and glass) were subject to various modes of edge loading. Preliminary observations revealed that crack growth and spalling tendencies were strongly dependent upon any non-uniformity in the loading. Localized (corner) loads generated cracks more readily than quasi-uniform, distributed, loads. These initial tests suggested a suitable geometry for model experiments to investigate such edge cracking
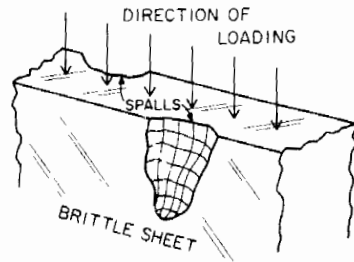
Fig. 1. A schematic illustration of an edge spall.

phenomena (Fig. 3). With this geometry the imposed stress was readily and accurately confined to a specific segment of the edge. This was done by applying load to an elevated region via a steel plate attached to the crosshead of a testing machine. Between the steel plate and test specimen, a soft inter-leaving material was placed to distribute the load evenly. A precrack was introduced into each plate, and aligned approximately parallel with the side surfaces. The load was applied at a uniform rate of $\sim 100 \, \text{Ns}^{-1}$ and the cracks optically monitored throughout the experiment.

Stability of the specimen was achieved by clamping it between thick plates with rubber interlayers (Fig. 3). This arrangement inhibited buckling, while allowing a stabilizing moment to be exerted by means of shear tractions distributed along the side faces (Fig. 4). However, friction may have developed at the loading area, creating a lateral force (Fig. 4) and influencing on the cracking behavior.

2.2. Observations

Crack propagation was observed to occur in three stages. Initial extension of the crack (Stage I) was unstable and accompanied by a small load drop (Fig. 5). Subsequent growth (Stage II) was stable, occurring at a constant load L. By this stage, the crack had progressed into a trajectory parallel to the side surface at a characteristic depth, d, beneath the surface. This depth was independent of the location
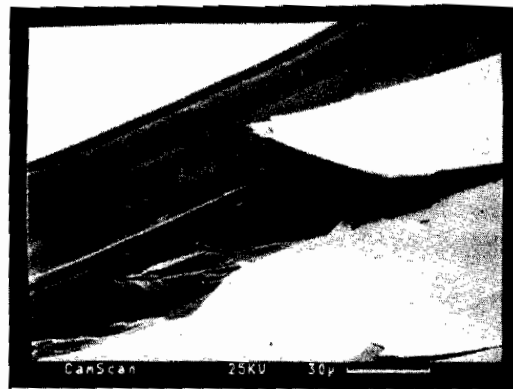
of the precrack (Figs 3 and 6). Finally, in Stage III, the crack deviated to the free surface, creating a spall (Fig. 6), and the load dropped to zero. The spalls exhibited a characteristic ratio (length divided by thickness), R, which for PMMA had values in the range, $R = 6 \pm 1$.

Measurements of the stable propagation load indicated that the load per unit thickness, P, exhibited a systematic variation with the characteristic crack depth d (Fig. 7) such that

$$P \equiv L/b$$
$$\approx A \sqrt{d}. \qquad (1)$$

The characteristic depth also revealed a unique dependence on the distance between the load line and the free surface, h (Fig. 3) such that (Fig. 8)

$$d = Bh. \qquad (2)$$

The values of the coefficients A and B are summarized in Table 1. These coefficients provide the basis for comparison with crack growth predictions, as discussed in Section 5.
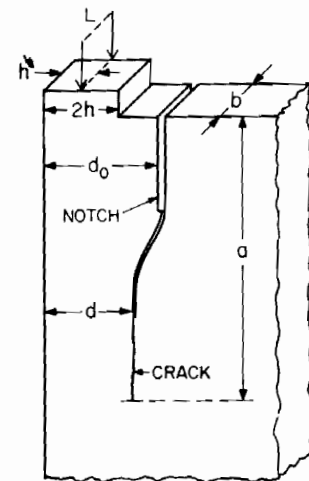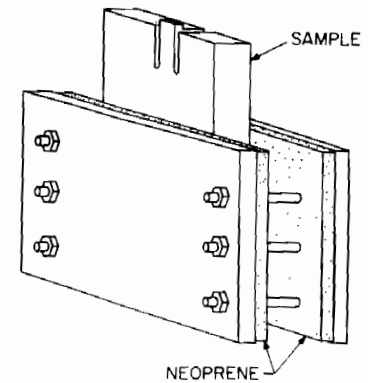

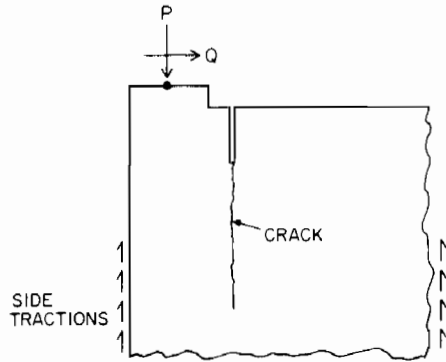Fig. 3. Schematic drawing of the test specimen used to study edge cracking and spalling.

Fig. 2. A scanning electron micrograph of a Cr film decohering from a glass substrate. (Courtesy of R. M. Fisher.)

Fig. 4. Schematic illustrating the system of forces exerted on the test specimen by the applied load and the constraining plates.

3. BASIC EDGE CRACK PROBLEMS
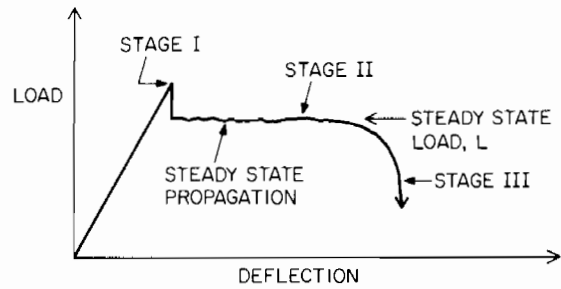
An important edge fracture problem, depicted in Fig. 9, consists of a plate containing a plane crack of length a at a depth d beneath the free surface (Fig. 9). The beam above the crack is subject to a uniform compressive stress, σ, parallel to the crack (or, equivalently, a load per unit thickness P, exerted at a line of action, $d/2$ below the surface). The stress state for this configuration is mixed mode, characterized by stress intensity factors, K_I and K_{II}. Some trends in K with crack length can be ascertained using finite element computations,† as summarized in Fig. 9. Such computations reveal that each stress intensity factor increases monotonically and eventually attains a steady state. General trends in edge cracking are thus most expeditiously addressed by using *analytic* approaches to obtain asymptotic solutions for both short ($a \ll d$) and long ($a \gg d$) cracks. These solutions, derived below, are shown to provide adequate representations of K_I and K_{II} for cracks having lengths, $a \lesssim d/4$, and $a \gtrsim 4d$, respectively (Fig. 9).

3.1. Asymptotic results for long cracks

The long crack problem (Fig. 10) involves a semi-infinite crack, parallel to the free surface of a semi-infinite, isotropic, elastic planar body. The only length quantity in the problem is the distance d between the crack and the surface. The cracked "arm" is subject to a compressive load P acting through the center of the arm, and a moment M (both being defined per unit thickness perpendicular to the plane).

Far from the crack tip, the arm is subject to a combined state of bending and compression. Exact results for the energy release per unit advance of the crack are thus readily obtained using simple energy
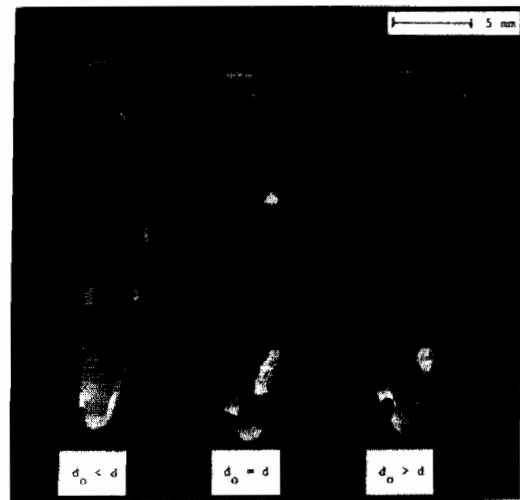
---

†The finite element results were calculated using 8-node, isoparametric, plane-strain quadrilateral elements (the MARC finite element package). The stress intensity factors were obtained from crack surface displacements near the crack tip.

Fig. 5. Typical load displacement curve.

Fig. 6. Optical views of spalled segments of PMMA, indicating the essential constancy of the relative steady state crack depth, d (independent of d_0).
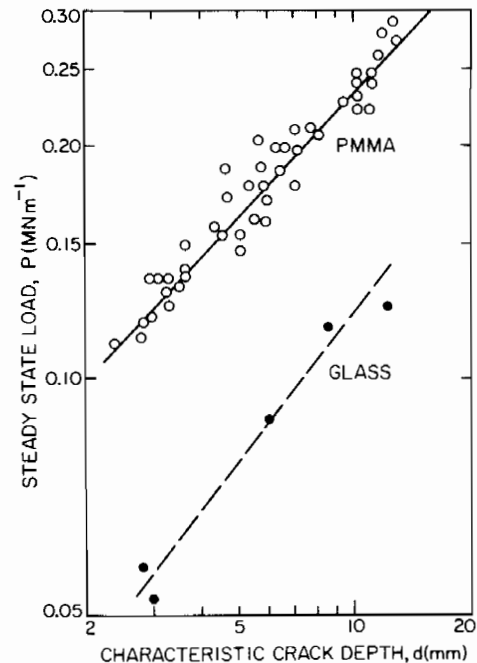

Fig. 7. Trends in steady state load P, with characteristic crack depth d for PMMA and glass.
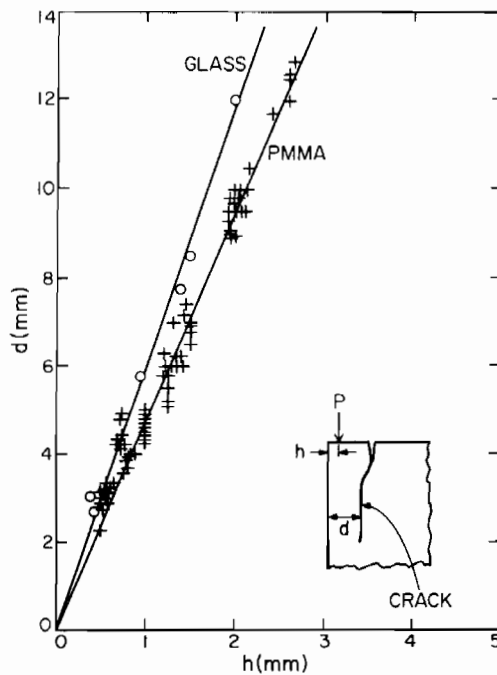
Fig. 8. Trends in characteristic crack depth d with load line depth h.

arguments [4, 5], these give

$$G = \left[P^2 + 12\left(\frac{M}{d}\right)^2 \right] \Big/ 2\hat{E}d \qquad (3)$$

where $\hat{E} = E$ in plane stress and $\hat{E} = E/(1 - v^2)$ in plane strain.

For arbitrary combinations of P and M the stress field at the crack tip is governed by both K_I and K_{II}. Dimensional considerations require that the stress intensity factors be related to the load quantities by

$$K_I = c_1 Pd^{-1/2} + c_2 Md^{-3/2}$$
$$K_{II} = c_3 Pd^{-1/2} + c_4 Md^{-3/2} \qquad (4)$$

---

†For the case indicated in Fig. 10, where a compressive load has its line of action a distance h below the surface.
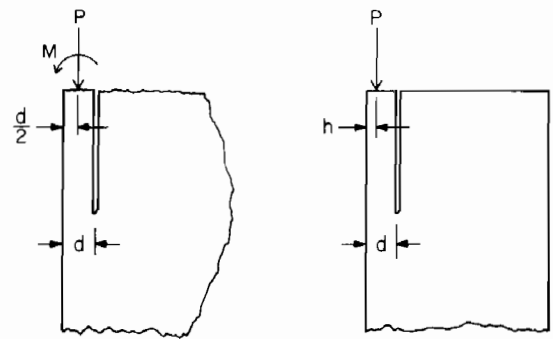

Fig. 10. Idealized geometry and loading for Stage II crack advance, including definition of M and P.

where the c_i are constants. Furthermore, since the energy release rate is given by

$$G = (K_I^2 + K_{II}^2)/\hat{E} \qquad (5)$$

comparison of equations (3) and (5) reveals that the constants must satisfy

$$c_1^2 + c_3^2 = \tfrac{1}{2}, \quad c_1 c_2 + c_3 c_4 = 0, \quad c_2^2 + c_4^2 = 6. \qquad (6)$$

Specific determination of c_i requires that the crack problem be rigorously solved for one loading combination. This has been done for the case $M = 0$ (Appendix I), giving

$$c_1 = 0.434, \quad c_2 = 1.934,$$
$$c_3 = 0.558, \quad c_4 = -1.503. \qquad (7)$$

The corresponding values of K_I and K_{II} for a crack at depth d, subject to uniform edge compression, are indicated on Fig. 9: denoted "long crack asymptotes". Corresponding trends in K_I and K_{II} with crack depth are summarized in Fig. 11.† Note that K_I exhibits a maximum at $d = 4.1\,h$, and $K_{II} = 0$ at $d = 7.8\,h$. Also plotted on Fig. 11 are the finite element solutions. The discrepancy between the analytic and finite element results for K_{II} has been identified as being caused by the finite geometries of the finite element solution.
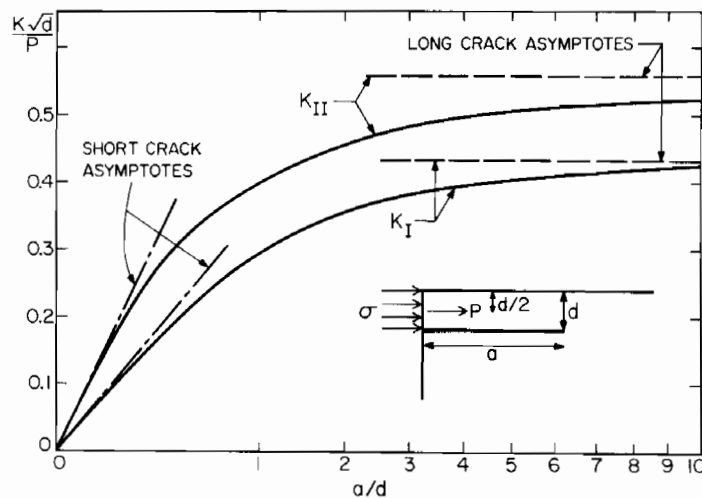

Fig. 9. Trends in K_I and K_{II} as a function of crack length for a crack having the indicated configuration.
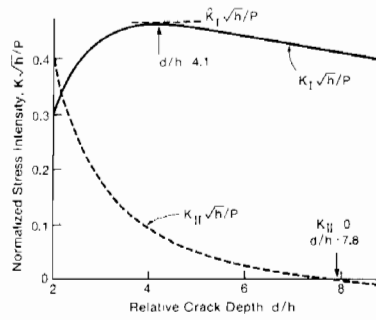
Fig. 11. Trends in K_I and K_{II} as a function of crack depth for a semi-infinite crack and the loading geometry defined in Fig. 3.

Fig. 12. The effects of K_{II} on the crack path in a brittle solid.

4. COMPARISON BETWEEN THEORY AND EXPERIMENT

The experimental result deemed to have the most fundamental significance concerns the existence of the *characteristic* steady-state *crack depth, d.* The location of this trajectory is presumed to be dictated by the condition, $K_{II} = 0$, because experiments on brittle solids [9] indicate that a planar crack only continues to advance in its own plane when the crack tip is subject to pure mode I: *positive* K_{II} deflects the crack *away* from the side surface, while *negative* K_{II} causes the crack to deviate *toward* the surface (Fig. 12). For preliminary comparison of this premise with experiment, the Stage II crack propagation process is idealized (Fig. 10), as a combination of P and M, with

$$M = P(d/2 - h). \tag{13}$$

Hence, by setting $K_{II} = 0$ in equation (4) and substituting M from equation (13), steady-state crack propagation is predicted to occur at a load

$$\frac{P}{K_{Ic}\sqrt{d}} = \frac{1}{c_1 - c_2 c_3/c_4} \equiv 0.87 \tag{14}$$

and at a depth

$$d/h = 7.8. \tag{15}$$

Comparison with the experimental results [equations (1) and (2) and Table 1] indicates consistency of functional form, with $A \equiv 0.87 K_{Ic}$ and $B \equiv 7.8$. However, appreciable numerical discrepancies exist (Table 1); notably, the predicted values of A are too small and the predicted B is too large.

The discrepancy is *not* resolved either by regarding the crack path as the trajectory having the maximum global, coplanar strain energy release rate (because this path occurs at $d = 2$ h) or by any other simple crack growth criterion (such as the maximum K_I criterion discussed below). Furthermore, the results cannot be rationalized by simply invoking an unknown additional moment deriving from the constraining plates, from load misalignment, etc. because a moment that brings d/h closer to the observed value (positive sign) invariably causes the predicted load to deviate further from the measured load (and vice versa). There are believed to be three possible contributions to the discrepancy. One arises from the

3.2. Asymptotic results for short cracks

The stress intensity factors for short cracks may be obtained from the surface stresses (Appendix II), as [6]

$$K_I \approx 1.12\sigma_{yy}\sqrt{\pi a}$$
$$K_{II} \approx 1.12\sigma_{yx}\sqrt{\pi a}. \tag{8}$$

Specifically, for short cracks at depth d, subject to uniform edge compression

$$\frac{K_I\sqrt{d}}{P} = 0.36\sqrt{(a/d)}$$

$$\frac{K_{II}\sqrt{d}}{P} = 0.63\sqrt{(a/d)} \tag{9}$$

as indicated on Fig. 9: denoted "short crack asymptote".

The surface stresses may also be used to estimate trends in the crack activation load, by requiring that fracture initiates from a distribution of pre-existing edge flaws. Then, weakest link concepts [7] suggest that the fracture probability Φ may be expressed as

$$-\ln(1 - \Phi) = \int_{2h}^{\infty} \left[\frac{\sigma_{yy}}{S_0}\right]^m \frac{dx}{h_0} \tag{10}$$

where m, S_0 and h_0 are parameters that characterize the flaw population. Noting that, to a reasonable approximation (Appendix II, Fig. B1)

$$\sigma_{yy} \approx \frac{4}{(\pi^2 - 4)}\left[\frac{P}{x}\right] \tag{11}$$

the fracture load, at the median probability level ($\Phi = \frac{1}{2}$) may be readily derived as

$$P_c = \frac{m-1}{m}(\ln 2)^{1/m}\frac{(\pi^2 - 4)}{4}\xi_0(2h)^{(m-1)/m} \tag{12}$$

where $\xi_0 = S_0 h_0^{1/m}$. The fracture load is thus predicted to scale almost linearly with h. This scaling law is similar to Auerbach's law [8] that describes crack initiation at spherical indentations in brittle surfaces, and consistent with practical experience that thin spalls initiate more readily than thick ones.
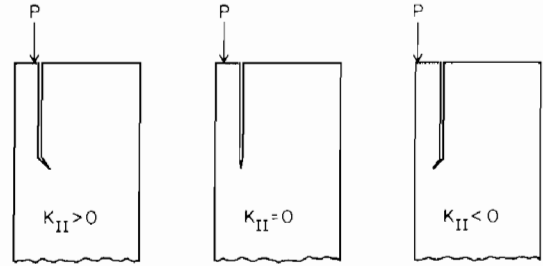
Table 1. Crack propagation constants

Material	K_{Ic} (MPa$\sqrt{m}$)	Loading coefficient A (MPa$\sqrt{m}$)		crack depth coefficient B		
		Measured	Predicted ($K_{II} = 0$)	Measured	Predicted $K_{II} = 0$	K_I maximum
PMMA	~1.0	2.4	~0.9	4.8	7.8	4.1
Glass	~0.6	0.9	~0.5	6.0	7.8	4.1

loading configuration, the others from the specimen geometry. A lateral force, Q, develops at the loading line [Fig. 4(b)], as the specimen attempts to rotate in response to the imposed moment, M. Beam theory (Appendix III) indicates that such a lateral force induces crack surface displacement having a different functional form than those induced by the moment, resulting in crack surface contact (Fig. 13). Friction at this contact would inhibit full transmission of the imposed K_{II} to the crack tip, causing the crack plane to become *closer* to the surface than the above prediction (based only on P and M). Furthermore, the frictional tractions would tend to counteract the axial force P and thus require *larger applied loads* to achieve crack extension. Both of these trends are consistent with the observed deviations from equations (14) and (15). The analysis needed to quantify the implied frictional effect is, however, beyond the scope of the present article.

For completeness, it is noted that the experimentally measured values of the crack depth, d (Table 1) fall between the value predicted at $K_{II} = 0$ and the value when K_I exhibits a maximum, $\hat{K}_I$. However, use of a maximum K_I as a fracture criterion is deemed inappropriate in the present context, because K_{II}/K_I is substantial at $K_I = \hat{K}_I$ (Fig. 11). The crack would thus tend to deviate from its plane at this location as illustrated in Fig. 12, and the observed steady state behavior could not obtain.

Edge *spalling* is attributed to the onset of elastic buckling, because buckling induces substantial nega-
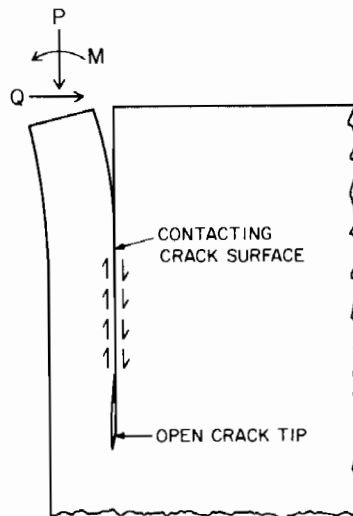
tive K_{II} and thereby deflects the crack to the surface (see Fig. 12). The buckling instability initiates at a critical axial load [10]

$$P_c = \lambda E \left(\frac{d}{a}\right)^2 d \tag{16}$$

where λ is a constant that depends on the boundary conditions. The two extreme values pertinent to the present problem are $\pi^2/3$ (rotation inhibited) and $\pi^2/48$ (one free end). By substituting P from equation (14), into equation (16) a critical aspect ratio for spalling emerges

$$\left(\frac{a}{d}\right)_c \approx \left[\frac{\lambda E \sqrt{d}}{K_{Ic}}\right]^{1/2}. \tag{17}$$

For typical values of d pertinent to the present experiments (~1 mm) the spall ratio measurements (Section 2.2) indicate a value of $\lambda = 0.4 \pm 0.1$. This value lies within the expected range, being somewhat in excess of the free end result ($\lambda \approx 0.18$). Some lateral constraint is thus implied, consistent with the preceding interpretation of the discrepancy between the measured and predicted values of the crack path and steady state load.

5. CONCLUDING REMARKS

The research presented in this article provides the background needed to analyze and predict the edge cracking and spalling behavior encountered in many situations having practical importance. In particular, it is now apparent that, by separating the imposed loads (mechanical or thermal) into force and moment components, the relative mode I and mode II stress intensities can be readily specified. Then, comparisons with measurements of crack trajectories and of crack extension loads allow definition of the criteria that dictate various aspects of edge cracking.

The present study has been restricted to homogeneous materials. However, extension to heterogeneous systems would be straightforward. In particular, re-evaluation of K_I and K_{II} for heterogeneous systems would address such important phenomena as the decohesion of thin films from substrates, delamination cracking in composites, etc.

The present comparison between experiment and theory has revealed that the loading used to conduct the experiments is complex, because lateral restraining tractions may develop at the load line. Experimental measurements using designs that permit free rotation of the specimen and thereby inhibit the development of such tractions are now in progress.

Fig. 13. A schematic illustration of the partial crack surface contact expected when a lateral force Q develops due to friction at the load line.

REFERENCES

1. A. G. Evans, A. C. Palmer, D. J. Goodman, M. F. Ashby, J. W. Hutchinson, A. R. S. Ponter and G. J. Williams, *AHR Ice Symposium*, Hamburg (1984).
2. J. G. Fonseca, J. D. Eshelby and C. Atkinson, *Int. J. Fract. Mech.* **7**, 421 (1971); B. Cotterell, J. Kamminga and F. P. Dickson, *Int. J. Fract.* **29**, 205 (1985).
3. R. M. Cannon, R. Fisher and A. G. Evans, *Decohesion of Thin Films from Ceramics, Proc. Symp. on Thin Films-Interfaces and Phenomena*, Boston, Mass. Mater. Res. Soc. (1986).
4. K. Kendall, *Proc. R. Soc.* **A361**, 245 (1978).
5. J. D. Eshelby, The calculation of energy release rates, In *Prospects in Fracture Mechanics*, (edited by G. C. Sih *et al.*). Noordhoff, The Netherlands (1974).
6. G. C. Sih, *Handbook of Stress Intensity Factors*. Inst. Fracture and Solid Mechanics, Lehigh University, Bethlehem, Pa (1973).
7. W. Wiebull, *J. appl. Mech.* **18**, 293 (1951).
8. F. Auerbach, *Ann. Phys. Chem.* **43**, 61 (1891).
9. F. Erdogan and G. C. Sih, *J. Basic Engng, Trans. A.I.M.E.* **85D**, 519 (1963).
10. S. P. Timoshenko and J. M. Gere, *Theory of Elastic Stability*, 2nd edn. McGraw-Hill, New York (1961).
11. C. J. Tranter, *Q. J. Mech. Appl. Math.* **1**, 125 (1948).
12. L. N. G. Filon, *Proc. R. Soc. Edin.* **49**, 38 (1928–9).

APPENDIX I

Stress intensity factors for a semi-infinite sub-surface crack

In this Appendix we set up and solve the integral equation for the plane strain problem specified in Fig. A1.

Let $b_x(\xi)$ and $b_y(\xi)$ be the x and y components of an edge dislocation located on the x-axis at $x = \xi$ and interacting with a traction-free boundary along $y = 1$. The stress components $\sigma_{yy}(x)$ and $\sigma_{xy}(x)$ at a point $(x, 0)$ on the x-axis induced by the dislocation at $(\xi, 0)$ can be obtained using Muskhelishvili methods and are given by

$$\sigma_{yy}(x) + i\sigma_{xy}(x) = 2\bar{B}(\xi)(x - \xi)^{-1}$$
$$+ B(\xi)G_1(x - \xi) + \bar{B}(\xi)G_2(x - \xi) \quad (A1)$$

where $i = \sqrt{-1}$, ($\bar{\ }$) denotes the complex conjugate, and

$$G_1(\zeta) = -16\zeta/(4 + \zeta^2)^2$$

$$G_2(\zeta) = -2\zeta/(\zeta^2 + 4) + 8/(\zeta - 2i)^3$$

$$B(\xi) = E[b_x(\xi) + ib_y(\xi)]/[8\pi i(1 - v^2)].$$

The semi-infinite crack is represented by a distribution of dislocations lying along the negative x-axis such that the traction vanishes along the negative x-axis. That is, the
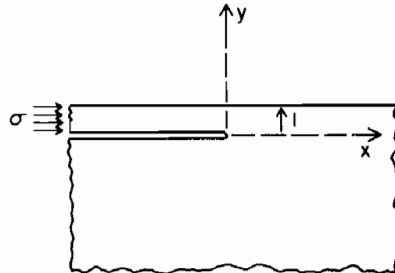

Fig. A1

distribution of dislocations $B(\xi)$ for $\xi \leqslant 0$ must satisfy

$$2\int_{-\infty}^{0} \bar{B}(\xi)(x - \xi)^{-1} d\xi + \int_{-\infty}^{0} [B(\xi)G_1(x - \xi)$$
$$+ \bar{B}(\xi)G_2(x - \xi)] d\xi = 0 \quad (A2)$$

for $x \leqslant 0$, where the first integral is the Cauchy principal value integral.

The crack opening displacement components are defined in the usual way as $\delta_x = u_x(x, 0^+) - u_x(x, 0^-)$ and $\delta_y = u_y(x, 0^+) - u_y(x, 0^-)$ for $x < 0$, and they are related to the dislocation distribution by

$$\delta_x(x) + i\delta_y(x) = \int_{x}^{0} [b_x(\xi) + ib_y(\xi)] d\xi$$
$$= \frac{8\pi i(1 - v^2)}{E} \int_{x}^{0} B(\xi) d\xi. \quad (A3)$$

The stress state remote from the origin in the "arm" (i.e. in $0 < y \leqslant 1$ for $x \to -\infty$) is prescribed to be $\sigma_{xx} = -\sigma$ (with $\sigma_{zz} = -v\sigma$) so that $\epsilon_{xx} = -(1 - v^2)\sigma/E$. For $x \to -\infty$

$$d\delta_x/dx = u_{x,x}(x, 0^+) = \epsilon_{xx} = -(1 - v^2)\sigma/E$$

since $u_{x,x}(x, 0^-) \to 0$ as $x \to -\infty$. Thus, from (A3)

$$b_x = -d\delta_x/dx = (1 - v^2)\sigma/E \quad \text{as} \quad \xi \to -\infty \quad (A4)$$

and

$$\text{Im}\{B\} = -\sigma/(8\pi) \quad \text{as} \quad \xi \to -\infty. \quad (A5)$$

Note that b_y is related to the crack opening displacement by $b_y = -d\delta_y/dx$. Since $d\delta_y/dx$ is not known *a priori* for large negative x, the real part of B is unknown for large negative ξ; it must be determined as part of the solution to the integral equation. Condition (A5), together with the requirement that $B(\xi)$ has an inverse square root singularity at $\xi = 0$, complete the specification of the integral equation (A2) for $B(\xi)$. A direct calculation shows that the stress intensity factors are given by

$$K_I + iK_{II} = (2\pi)^{3/2} \lim_{\xi \to 0-} \{(-\xi)^{-1/2} \bar{B}(\xi)\}. \quad (A6)$$

To prepare the integral equation for numerical solution, make the changes of variables

$$x = (u - 1)/(u + 1)(-1 < u < 1),$$
$$\xi = (t - 1)/(t + 1)(-1 < t < 1). \quad (A7)$$

The integral equation can then be rewritten as

$$\int_{-1}^{1} \bar{A}(t)(u - t)^{-1} dt + \int_{-1}^{1} \{A(t)G_1(x - \xi)$$
$$+ \bar{A}(t)[1 + t + G_2(x - \xi)]\}(1 + t)^{-2} dt = 0 \quad (A8)$$

where $A(t) \equiv B(\xi)$ and $x - \xi = 2(u - t)/[(1 + u)(1 + t)]$. The representation for $A(t)$ was taken to be

$$A(t) = \frac{1}{\sqrt{1 - t}} \left\{ a_0 + (1 + t) \sum_{k=1}^{N} a_k T_{k-1}(t) \right\} \quad (A9)$$

where $T_j(t)$ is the Chebyshev polynomial of the first kind of degree j and the a's are complex coefficients which must be determined in the solution process. From (A5), $\text{Im}\{a_0\} = -\sqrt{2}\sigma/(8\pi)$, while the real part of a_0, $\text{Re}\{a_0\}$, and the real and imaginary parts of a_k for $k = 1, N$ are unknown.

When substituted into (A8), the representation for A leads to an equation of the form

$$\sum_{k=1}^{N} [a_k I_1(u, k) + \bar{a}_k I_2(u, k)] + \text{Re}\{a_0\}I_3(u) = \sigma I_4(u) \quad (A10)$$

where the terms I_1 to I_4 involve integrals such as

$$I_1(u, k) = \int_{-1}^{1} G_1(x - \xi)T_{k-1}(t)(1 + t)^{-1}(1 - t)^{-1/2} dt.$$

These integrals must be evaluated numerically for given values of u and k. (Some of the integrals require further

Table A1. Computed values of c_1 and c_3 where (A10) is satisfied at the N Gauss–Legendre points

N	c_1	c_3	$c_1^2 + c_3^2$
6	0.43594	0.55754	0.50089
8	0.43383	0.55828	0.49988
12	0.43418	0.55811	0.49999

reduction before they can be efficiently evaluated numerically.)

The solution procedure is as follows. Let a set of $2N$ real unknowns be $\mathrm{Re}\{a_0\}$ plus the real and imaginary parts of a_k for $k = 1, N$, excluding the imaginary part of a_N (i.e. effectively, $\mathrm{Im}\{a_N\}$ is set to zero). This set of $2N$ unknowns is used to satisfy the real and imaginary parts of (A10) at N points $\{u_i\}$ on the interval $-1 < u < 1$. The results tabulated above were determined using Gauss–Legendre points for $\{u_i\}$. However, several other sets of points were tried and the results for c_1 and c_3 were not strongly influenced by this choice. Considerable care must be taken to ensure that the integrals involved in the I_j are evaluated accurately. A convergence study was made for each entry in the table so that the results listed were free of any dependence on inaccuracies in the numerical evaluation of the integrals. Once the a's have been determined, the stress intensity factors can be computed, using (A6) and (A9), from

$$K_1 + iK_{II} = 2\pi(\pi)^{1/2}\left\{\bar{a}_0 + 2\sum_{k=1}^{N} \bar{a}_k T_{k-1}(1)\right\}. \quad \text{(A11)}$$

The crack opening displacements can be computed from

$$\delta_x(x) + i\delta_y(x) = 16\pi E^{-1}(1-v^2)i\sqrt{1-u}$$
$$\times \int_{-1}^{1}\left[a_0 + (1+t)\sum_{k=1}^{N}a_k T_{k-1}\right](1+t)^{-2}\,d\eta \quad \text{(A12)}$$

where t is related to the integration variable η by $t = 1 - (1-u)(1-\eta)^2/4$ and where x and u are still related by (A7).

The general expressions for K_1 and K_{II} in equation (4) apply to the present case with $M = 0$, $d = 1$ and $P = \sigma$ so that $K_1 + iK_{II} = (c_1 + ic_3)\sigma$. The computed results for c_1 and c_3 are presented in Table A1 for 3 choices of N. Also included is the computed value of $c_1^2 + c_3^2$ which by equation (6) should be precisely $1/2$; this value provides an independent check on the accuracy of the solution. Based on the convergence displayed by the data in Table A1 and on some additional convergence studies, we believe that the values of c_1 and c_3 given by equation (7) are accurate to within 0.2%.

The values of c_2 and c_4 follow immediately from equation (6) and must therefore have essentially the same degree of accuracy.

For completeness, we show the crack opening displacements in Fig. A2 for the case considered here (i.e. $M = 0$). Finally, it can be mentioned that the results for the stress intensity factors hold for plane stress as well as plane strain, and the plots in Fig. A2 for the crack opening displacements hold for plane stress if $(1 - v^2)$ is replaced by 1 in the ordinate variable.

APPENDIX II

Stress fields: small crack asymptotics

Unstable propagation of small cracks can be analyzed by considering the top face of a quarter-plane loaded by an applied compressive stress of magnitude σ up to a distance d from the corner, using the method developed by Tranter [11]. The radial (σ_r), tangential (σ_θ) and shear ($\tau_{r\theta}$) stresses are given by

$$\frac{r}{h}(\sigma_\theta - \sigma_r)$$
$$= \sigma\left\{\frac{2\alpha\sin(\alpha-\theta) - \sin 2\alpha\sin(\alpha+\theta)}{4\alpha^2 - \sin^2 2\alpha}\right\}$$
$$- \frac{\sigma}{\pi}\int_0^\infty [P(\xi) - S(\xi)]\sin\{\xi\log(d/r)\}\,d\xi. \quad \text{(B1a)}$$

$$\frac{r}{h}(\sigma_\theta + \sigma_r)$$
$$= -\sigma\left\{\frac{2\alpha\sin(\alpha-\theta) - \sin 2\alpha\sin(\alpha+\theta)}{4\alpha^2 - \sin^2 2\alpha}\right\}$$
$$+ \frac{\sigma}{\pi}\int_0^\infty [P(\xi) - \xi Q(\xi) - S(\xi) + \xi T(\xi)]$$
$$\times\frac{\sin\{\xi\log(d/r)\}}{1+\xi^2}\,d\xi - \frac{\sigma}{\pi}\int_0^\infty [Q(\xi) + \xi P(\xi)$$
$$- T(\xi) - \xi S(\xi)]\frac{\cos\{\xi\log(d/r)\}}{1+\xi^2}\,d\xi. \quad \text{(B1b)}$$

$$\frac{r}{h}\tau_{r\theta} = \frac{\sigma}{2\pi}\int_0^\infty [R(\xi) - U(\xi)]\cos\{\xi\log(d/r)\}\,d\xi \quad \text{(B1c)}$$

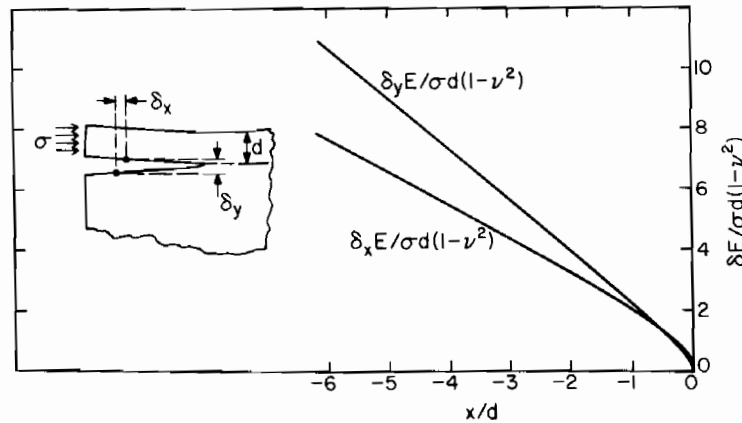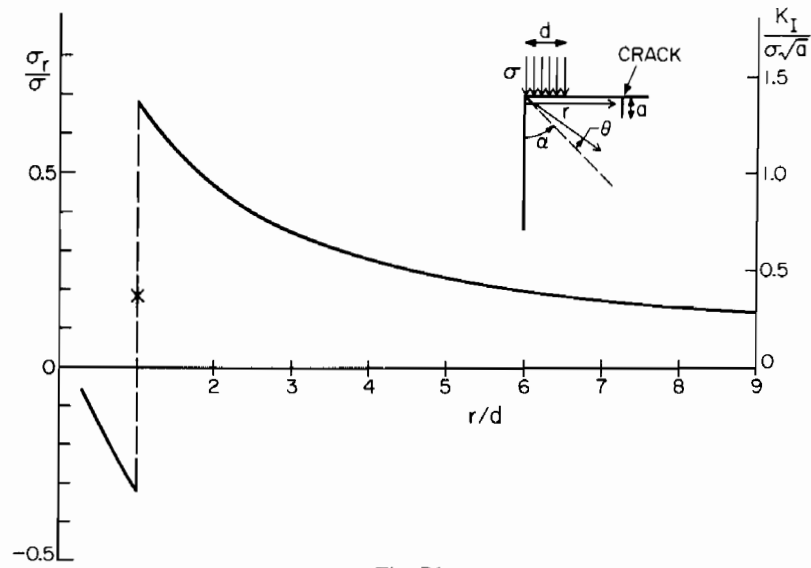where $\alpha = \pi/4$ and $P(\xi)$, $Q(\xi)$ and $R(\xi)$ are the symmetric

Fig. A2

Fig. B1

parts of the solution given by

$$[\xi \sin 2\alpha + \sinh 2\alpha\xi]P(\xi) = \sin(\alpha - \theta)\cosh[(\alpha + \theta)\xi]$$
$$+ \sin(\alpha + \theta)\cosh[(\alpha - \theta)\xi].$$

$$[\xi \sin 2\alpha + \sinh 2\alpha\xi]Q(\xi) = \cos(\alpha - \theta)\sinh[(\alpha + \theta)\xi]$$
$$+ \cos(\alpha + \theta)\sinh[(\alpha - \theta)\xi].$$

$$[\xi \sin 2\alpha + \sinh 2\alpha\xi]R(\xi) = \sin(\alpha - \theta)\sinh[(\alpha + \theta)\xi]$$
$$- \sin(\alpha + \theta)\sinh[(\alpha - \theta)\xi].$$

and $S(\xi)$, $T(\xi)$ and $U(\xi)$ are the anti-symmetric parts of the solution given by

$$[\xi \sin 2\alpha - \sinh 2\alpha\xi]S(\xi) = \sin(\alpha - \theta)\cosh[(\alpha + \theta)\xi]$$
$$- \sin(\alpha + \theta)\cosh[(\alpha - \theta)\xi].$$

$$[\xi \sin 2\alpha - \sinh 2\alpha\xi]T(\xi) = \cos(\alpha - \theta)\sinh[(\alpha + \theta)\xi]$$
$$- \cos(\alpha + \theta)\sinh[(\alpha - \theta)\xi].$$

$$[\xi \sin 2\alpha - \sinh 2\alpha\xi]U(\xi) = \sin(\alpha - \theta)\sinh[(\alpha + \theta)\xi]$$
$$+ \sin(\alpha + \theta)\sinh[(\alpha - \theta)\xi].$$

The stresses can be determined by numerical integration [12]. The stresses along the top surface are calculated by letting $\alpha - \theta = \epsilon$ and then examining the limits of the above equations as $\epsilon \to 0$. Ignoring terms of order ϵ or smaller, the following stresses are obtained. At $r = d$: $\sigma_\theta = -\sigma/2$, $\tau_{r\theta} = \sigma/\pi$ and

$$\sigma_r = \left\{ \frac{12 - \pi^2}{\pi^2 - 4} \right\} \frac{\sigma}{2}. \tag{B2a}$$

At $r > d$, $\sigma_\theta = 0$, $\tau_{r\theta} = 0$ and

$$\left(\frac{r}{h}\right)\sigma_r = \left\{ \frac{4\sigma}{\pi^2 - 4} \right\} + \frac{2\sigma}{\pi} \int_0^\infty \left\{ \frac{\xi^2}{\sinh^2 \xi\pi/2 - \xi^2} \right\}$$
$$\times \frac{\sin\{\xi \log(r/d)\theta\}}{\xi} \, d\xi. \tag{B2b}$$

At $r < d$: $\sigma_\theta = \sigma$, $\tau_{r\theta} = 0$ and

$$\frac{r}{h}(\sigma_r + \sigma) = \left[\frac{4\sigma}{\pi^2 - 4} \right] - \frac{2\sigma}{\pi} \int_0^\infty \left\{ \frac{\xi^2}{\sinh^2 \xi\pi/2 - \xi^2} \right\}$$
$$\times \frac{\sin\{\xi \log(d/r)\}}{\xi} \, d\xi. \tag{B2c}$$

The surface stresses deduced from equation (B2) are plotted in Fig. B1.

APPENDIX III

Beam theory analysis of crack surface contact

In the absence of a lateral restoring force, the opening displacement of the crack surface has the form

$$w_m(z) = \frac{Mz^2}{2EI} \tag{C1}$$

where z is the distance from the crack tip. However, when a restoring force Q is imposed, the surface displacements must be modified by

$$w_q(z) = \frac{-Qz^2(3a - z)}{6EI}. \tag{C2}$$

The resultant displacement is thus

$$w(z) \equiv w_m(z) + w_q(z) = \frac{z^2}{2EI}\left[(M - Qa) + \frac{Qz}{3} \right]. \tag{C3}$$

The parenthetical term containing z indicates that w can change sign along the crack path, when w is initially negative, at small z ($Qa > M$). However, it is also noted that, near the crack tip, the crack tip region remains open, even though contact may exist over the central portion of the crack (Fig. 13).